Spatially extended radiant heat fire model

Jenna S. McDanold [*]

Earth and Environmental Sciences Division, Los Alamos National Laboratory, Los Alamos, New Mexico 87545, USA
and School of Mathematical Sciences, Rochester Institute of Technology, Rochester, New York 14623, USA

Nishant Malik

School of Mathematical Sciences, Rochester Institute of Technology, Rochester, New York 14623, USA

Recent wildfire prevalence and destruction have led to new initiatives in the search for better land management techniques and prescriptions for controlled burns. With limited data on low-intensity prescribed burns, finding models that can represent fire behavior is of great importance to learning how to control fires with more accuracy while also maintaining the purpose for the burn, be it reducing fuels or managing the ecosystem. Here we use a data set of infrared temperatures collected in the New Jersey Pine Barrens from 2017 through 2020 to develop a model for very fine-scale fire behavior (≈ 0.05 m^2). The model uses distributions from the data set to define five stages in fire behavior in a cellular automata framework. For each cell, the transition between each stage is probabilistically driven based on the radiant temperature values of the cell and its immediate neighbors in a coupled map lattice. With five distinct initial conditions, we performed 100 simulations and used the parameters derived from the data set to develop metrics for model verification. To validate the model, we also expanded it to include variables not in the data set that are important for fire behavior, e.g., fuel moisture levels and spotting ignitions. The model matches several metrics compared to the observational data set and exhibits behavioral characteristics expected from low-intensity wildfire behavior including a long and varied burn time for each cell after initial ignition, and lingering embers in the burn zone.

I. INTRODUCTION

Recent changes in weather and vegetation patterns have led wildfires to emerge as one of the biggest threats to human life and property in many parts of the world [1,2]. According to the National Interagency Fire Center website, the total number of acres burned in the United States has more than doubled from an average of 3.32 million acres per year between 1985 and 1990 to an average of 7.82 million acres per year between 2015 and 2020 [3]. The expansion of the wildland-urban interface increases the proximity of human structures and land to forest areas, raising the likelihood of humans being affected by these wildfires. In recent years, this expansion has led to an increase in wildfire destruction [4–6]. Furthermore, several decades of suppressing fires in these areas have also resulted in a negative effect on the fire-dependent ecosystems and the build-up of dry fuel on the ground [7,8].

To combat the devastation caused by these natural disasters, prescribed fires are an effective land management tool, provided we apply the correct prescription [9–12]. Currently, practiced fire experts rely on observation and experience for devising these prescriptions, but unforeseen circumstances can have disastrous results [13,14]. A rapid increase in technological tools since the early 1990s has given us a new way of fighting fires with information before a wildfire occurrence.

This information can be used to train new firefighters in the field and devise prescriptions for controlled burns that may mitigate the damage caused.

Process-based models such as FIRETEC, developed at the Los Alamos National Laboratory [15–17], or WFDS, developed in association with the National Institute of Standards and Technology [18,19], can offer us the opportunity to test various parameters for prescribed fires numerically, without the possibility of an escaping fire. These advanced tools also allow us to collect data on the simulations that would be challenging to gather in real-life fires [20]. These models are highly precise but require significant computing resources due to the use of computational fluid dynamics [17] and substantial technical manpower for their management. There exists a paramount need for low-complexity models which can provide reliable data to researchers and fire practitioners in real time.

As an alternative to these highly complex models, cellular automata (CA) models reduce the computational expense by discretizing time and space, reducing the model to a collection of basic equations applied to each cell during a single time step. Physicists often utilize the cellular automaton framework for representing geophysical processes that adhere to some basic physical laws in which the new value for a particular spatial location at time t depends on the spatial neighborhood at previous time steps [21–23]. From snow avalanche models [24] to lava flows [25] to porous media [26], CA models are popular among fluid flow modelers. The discretization

_____
[*]jennasmcd@lanl.gov

process resembles the act of using Reimann sums to calculate integral approximations. While some information may be lost in the estimation, the results can be close enough to be valuable depending on how and for what purpose you use the integral or model. CA models also often allow for the possibility of "self-reproduction" in that a neighboring state will directly reproduce itself in adjacent cells [21], a quality common in chaotic systems and fractals. Mathematical models are inherently approximations of the processes they represent, in which error estimates are used for validation purposes [27,28].

Most wildfire behavior CA models produce results that track the fire line and create images with limited information. They use information regarding the surrounding topography and wind data, seeking to predict the area burnt over time. The typical resulting graphs focus on either contours of the fireline in time increments as in Refs. [29–32] or they represent the shape of the resulting burnt area as in Refs. [5,33–35] or both [36]. These models take advantage of the discrete outputs in the CA framework, but this limits the information that can be obtained.

Our solution is to add an underlying coupled map lattice (CML) model to the CA framework. This additional step allows for more information to be collected than with typical CA models that only produce a finite amount of discrete output values. In this paper, we present a spatially extended radiant heat fire model (SERF), a CA model built from arrays with infrared radiant heat values recorded during a selection of small-scale prescribed fires. Using these infrared data, we determined the main characteristics of the radiant heat emanating from these fires and created a CML for simulating the fire behavior. We then used this CML to define five states of fire behavior of a CA model, creating a spatially extended discrete dynamical systems-based model whose parameters we determined from empirical data.

There have been many attempts at cellular automata models of fire behavior [5,31,35,37–39], but this is the first to incorporate a data set from prescribed fires performed outside of a laboratory. Using this data set, we determine the model's parameters, along with a targeted approach for the output, and validate the model's accuracy. The spread of the fire and radiant temperature are represented using probability distributions for various characteristics taken from the data set. The rest of this paper describes the model in Sec. II, the data set and parameters in Sec. III, and then the output and results in Sec. IV. Section V includes a summary and a description of future work.

II. DESCRIPTION OF THE MODEL

SERF defines $T_n(i, j)$, the radiant heat temperature at time step n for cell location (i, j), in five discrete stages. Using the CML framework, an equation defines the behavior of the radiant temperature for each stage, with parameter thresholds marking the transition from one stage to the next. These five stages represent the life cycle of radiant temperature for an area that burns. Figure 1 shows a schematic of the five stages and each are explained in detail in the following sections.
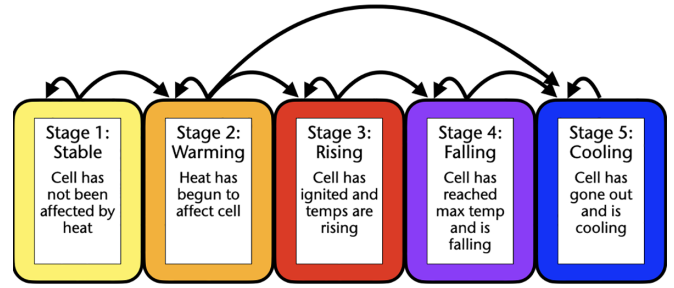

FIG. 1. A schematic of the five stages that make up the life cycle of a burning cell; a definition of the five cellular automata output states.

A. The model

All cells begin in stage one, *stable*, in which the heat from the oncoming fire has not yet reached this cell. Once that heat affects the cell, it transitions into the *warming* stage, and when the heat rises sufficiently for ignition, it transitions into stage three, *rising*. The heat then rises as the fuel is consumed until it reaches its maximum temperature, $T_M(i, j)$, after which it transitions into stage four, *falling*, when the radiant heat reduces as the fuel consumption completes. Once the fuel is gone, the flame ceases, and the cell transitions into stage five, *cooling*, in which the ground beneath the fire cools back to equilibrium with the ambient temperature of the area.

The parameters in SERF unique to each simulation are the domain size in two dimensions and the overall moisture content for the area, m_c. The parameters unique to each cell per simulation are the maximum radiant temperature $T_M(i, j)$, the heat transfer coefficient for the fuel $k(i, j)$, and the time required to rise to and fall from $T_M(i, j)$, $R(i, j)$, and $F(i, j)$, respectively. Each of these parameters are generated from a probability distribution built from the data set described in Sec. III A.

1. Algorithm structure and boundary conditions

The algorithm loops through each coordinate in the lattice, (i, j), defined by a domain size of $I \times J$ to calculate the radiant temperature and assign the discrete stage number to the cell. The first two stages calculate the radiant temperature of a particular cell using the temperatures of the surrounding neighbors. For this process, we use the Moore neighborhood defined for coordinate (i, j) as

$$N_{i,j} = (i + a, j + b)| - 1 \leqslant a, b \leqslant 1; a, b \in \mathbb{Z}. \quad (1)$$

In the event that a particular coordinate (i, j) lies on the boundary of the domain, we only consider those coordinates defined within the domain as part of the equations. Meaning, if we are calculating the ambient temperature of the corner coordinate $(1,1)$, then we would only consider the three existing neighbors, $(2, 1)$, $(2, 2)$, and $(1,2)$ in the calculation. For more information regarding the ambient temperature function, please see Sec. II A 2 and Eq. (3).

2. Stages one and two: Stability and warming

To begin, we initialize the entire domain as the base temperature for the day on which the burn is to take place, T_B,

which we define as stage one, stable. To start the fire, we synthetically raise the temperature to ignition for a chosen group of cells and set them to stage three, rising. As the heat from these initialized cells approaches the neighbors, radiant and convective heat transfer causes the temperature to rise and results in the transition into stage two. For stages one and two, we use a modified Newton's law of cooling equation to represent how the radiant temperature at time step $n + 1$ is affected by the ambient temperature of the neighboring area at time step n,

$$T_{n+1}(i, j) = T_n(i, j) + k(i, j)[A_n(i, j) - T_n(i, j)]. \quad (2)$$

Here $A_n(i, j)$ is the ambient temperature calculated from the neighboring cells with a weighting function $W(i, j)$ at the previous time step as follows:

$$A_n(i, j) = \sum_{a=-1}^{1} \sum_{b=-1}^{1} W(i + a, j + b)T_n(i + a, j + b). \quad (3)$$

If coordinate (i, j) is in stage one along with all of its neighbors, then we have $T_n(N_{i,j}) = T_B$ and $W(i, j) = 1/N$ for all i, j, where $N = \{N_{i,j}\}$ is the total number of cells in the calculation. This along with (3) leads to $A_n(i, j) = T_n(i, j)$ when all neighbors are of equal temperature. From (2), we therefore have $T_{n+1}(i, j) = T_n(i, j)$ and the temperature does not change. In stage two, since heat is present, we apply a multiplicative factor of 1.2 to $W(i, j)$, which represents the addition of convective heat transfer as the flames encroach on the area while the radiant temperature increases. Once the temperature rises to inside the bounds of the ignition interval such that $T_n(i, j) \in [I_{\min}, I_{\max}]$, a cell can undergo one of three options: (i) remain in stage two, warming; (ii) transition into stage three, rising; or (iii) transition into stage five, cooling. If $T_n(i, j) \in (I_{\min}, I_{\max})$, using the moisture content, m_c, then the cell attempts to ignite between $D_{\min}$ and $D_{\max}$ times, based on a uniformly distributed parameter delay matrix, D, which will be explained in detail in Sec. III C. If the attempt fails, then the cell remains in stage two. If the attempt succeeds, then the cell transitions into stage three. If we have $T_n(i, j) > I_{\max}$, then the cell automatically transitions into stage three, rising. If all attempts fail, then the cell transitions into stage five. A transition from stage two to stage five represents a cell that will not ignite due to the chemical structure of the fuel in that cell. For instance, this could represent a rock that will heat up but never ignite. Figure 2 shows how a particular cell might move through stages two to five, each of which is described in the subsequent subsections.

3. Stages three and four: Rising and falling

If the cell ignites, then the chemical and physical characteristics of the fuel become the driving forces in how the radiant heat rises and falls. Since the fuel is now being consumed, the area begins to generate its own heat. Thus, for stages three and four, we move away from Newton's law of cooling and define two linear functions for how the heat changes from one time step to the next. For stage three, rising, we have:

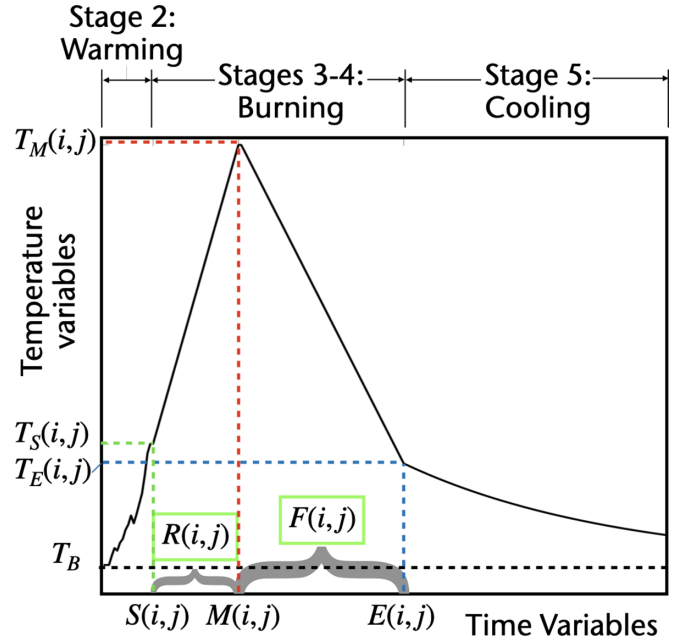$$T_{n+1}(i, j) = T_S(i, j) + \frac{T_M(i, j) - T_S(i, j)}{R(i, j)}[n - S(i, j)], \quad (4)$$

FIG. 2. Representation of how the radiant temperature changes in a specific cell over time beginning in stage two, warming, where Newton's law of cooling is applied, moving through the linear equations developed for stages three (rising) and four (falling) and ending in stage five, cooling; example of CML output for a single cell.

and for stage four, falling, we have:

$$T_{n+1}(i, j) = T_M(i, j) - \frac{T_M(i, j) - T_S(i, j)}{F(i, j)}[n - M(i, j)]. \quad (5)$$

For simplicity, stages three and four are defined as linear functions in which the cell rises to its maximum temperature, $T_M(i, j)$ over $R(i, j)$ time steps, and falls from $T_M(i, j)$ over $F(i, j)$ time steps. Since the temperature at which the transition into stage three occurs is not set but determined through the use of the delay matrix, $D(i, j)$ interacting with the ignition interval $(I_{\min}, I_{\max})$, we define $T_S(i, j)$ to be the ignition temperature for location (i, j) and $S(i, j)$ to be the time step at which the transition occurs. Then $M(i, j)$ is the time step at which the maximum temperature is achieved. During stage four, once the cell reduces in heat back down to the ignition interval, $[I_{\min}, I_{\max}]$, the cell is again tested to see if it has extinguished. The temperature at which the cell extinguishes is defined as $T_E(i, j)$ at time step $E(i, j)$, and we transition into stage five.

4. Stage five: Cooling

This stage represents the time when the fuel has been consumed, and the ground beneath the fuel is cooling off back down to equilibrium with the area's temperature, T_B. We use an exponential function to show how the heat dissipates after the fire has moved through the area:

$$T_{n+1}(i, j) = [T_E(i, j) - T_B] \exp\left[\frac{E(i, j) - n}{T_E(i, j) - T_B}\right] + T_B. \quad (6)$$
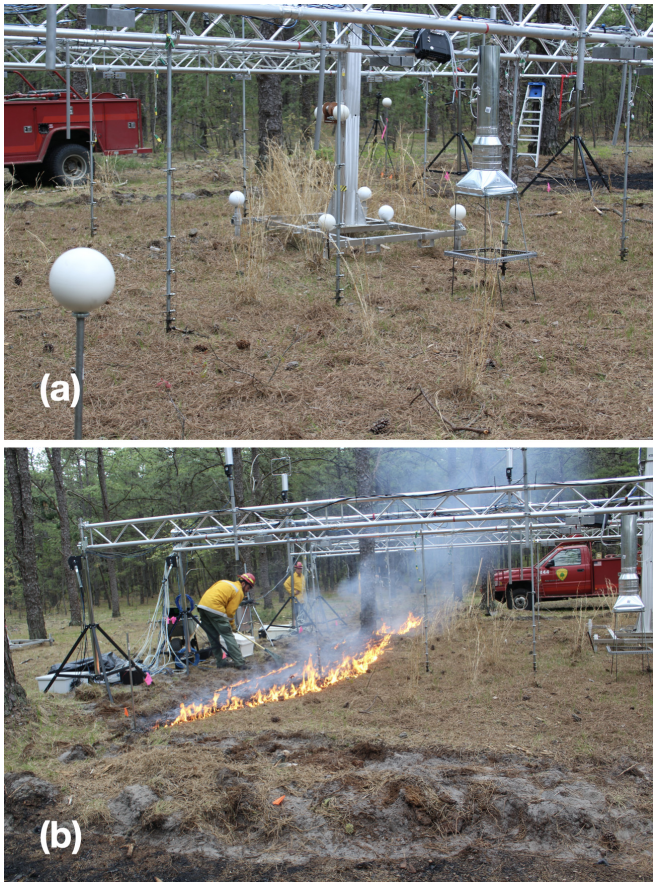
FIG. 3. Truss setup in the New Jersey Pine Barrens for the creation of the data set; (a) before the burn; (b) after burn was initialized (photos courtesy of Dr. Robert Kremens, Chester F. Carlson Center for Imaging Science, Rochester Institute of Technology (RIT); credit: USDA Forest Service Northern Research Station).

This is the last stage of the process. Once the cell reduces back down to T_B, it is considered to be burnt and is no longer subject to any temperature changes.

III. MODEL PARAMETERS AND THE DATASET

SERF was built from a large data set developed in the New Jersey Pine Barrens from 2017 through 2021 during several controlled burns, under a grant from Strategic Environmental Research and Development Program, within the Department of Defense. The data was collected by the Northern Research Station of the United States Department of Agriculture (USDA) Forest Service [40]. In this section, we describe the extent of the data set and how we incorporated this data into the model.

A. The data set

There were two types of fires that were burned under this grant: square fires with 12-m length sides and 30-acre fires. Both were prescribed and kept under tight surveillance. The 12-m fires were outfitted with a truss at 6 feet over the burning zone containing 16 equally spaced data collection devices in a 4-by-4 grid (see Fig. 3). Each device housed a FLIR
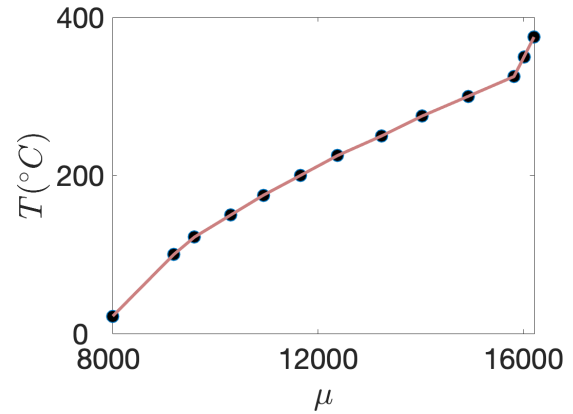

FIG. 4. Calibration graph for relating infrared output data to radiant temperature values from observations using a black box unit with the FLIR Lepton 1.5 camera.

Lepton 1.5 that recorded infrared information and a digital camera along with various other data collection devices. The fuel below the cameras for the 12-m burns was collected, weighed, and evenly distributed throughout the burn zone. For the 30-acre fires, the devices were distributed randomly throughout the burn zone.

All of the cameras were initiated simultaneously and began taking snapshots of the area at 1-s intervals. The FLIR Lepton 1.5 recorded the infrared radiant output (from 8 to 14 microns) emanating from each cell in the viewing range and outputted a numerical array with values ranging from approximately 8000 to 16 000. The prescribed fires were ignited below the cameras and allowed to burn through the area underneath [40]. For the 12-m burns, the viewing area for each camera was approximately 3 m square, but the resulting numerical array was presented as 60×80 cells. Figure 3 shows the setup for the data set collection. Please note that, due to the Covid-19 crisis, we could not perform the necessary experiments to determine the exact spatial region captured by each camera by calibrating the digital and infrared cameras together; this should be done in the future.

Since each segment of ground was individually recorded, we first found all of the arrays related to a particular fire in a given section and stacked the arrays on top of one another in a three-dimensional time-sequential tensor (dimensions being x and y spatial dimensions with time as the third). Of 3.1 million files, we could find 74 successful fire visualizations that did not have any deformities. We denote these 74 fire visualizations using the symbol f_m, where m is the fire index that goes from 1 to 74, that is the set $\{f_m\}_{m=1}^{74}$ represents these 74 successful fire visualizations.

From laboratory experiments performed with the Lepton camera, the infrared values were found to correspond to a radiant temperature flux range of approximately 22 °C to 400 °C [41]. For the interpolation scheme, we first attempted a cubic spline interpolation but the results were similar to the linear interpolation, and thus the linear was chosen for simplicity. Note the sudden increase toward the top right of the graph in Fig. 4 that indicates the temperature data may not be entirely accurate toward the upper bound for the range of temperatures recorded. This is reflected in the maximum temperatures for

the power flux being capped at $T_M = 400\,°\text{C}$. This anomaly was adjusted in the model so that some of the maximum temperatures can be above this value, but without accurate data for that range, it is possible that the resulting maximum radiant temperature estimations may be lower than the true values.

B. Data-driven parameters

From the data set, we obtained several parameters for SERF including two global parameters: the ignition interval, $[I_{\min}, I_{\max}]$, and the unburnt proportion of land $U(f_m)$ for a fire instance f_m and four cell-dependent input parameter matrices: the maximum temperatures, T_M, the rise and fall times, R and F, and the heat coefficients, k. Each of the input parameter matrices used in the model is defined using a probability distribution taken from all of the cells in the data-set fires. We experimented with fitting several different probability distributions to the data. Since we cannot assume that our data parameters adhere to any specific distribution, we chose the kernel distribution since it led to the most accurate model outputs compared to the observational data.

For R, F, T_M, and k, SERF builds the input matrices by assigning values to a subset of cells through sampling the corresponding distribution defined by the data set and then "smoothing" these numbers to increase realistic stability in the model. For R and F, a random number between 50% and 70% of the cells are assigned a value with the rest equal to 1. For k and T_M, all cells are assigned a value from their respective probability distributions.

The smoothing process for each of the four parameter matrices is performed by finding the sum of each cell and its immediate neighbors and then multiplying that by a random number chosen from a normal distribution:

$$P'(i, j) = p \sum_{a=-1}^{1} \sum_{b=-1}^{1} P(i + a, j + b), \quad (7)$$

where $P \in \{R, F, k, T_M\}$ and $p \sim \mathcal{N}(\mu = 1, \sigma = 0.04)$. This process is repeated twice for R, F, and k and 10 times for T_M. Then the values are normalized back to the original interval by finding the maximum value of the original matrix, $\max(P)$, and dividing that by the maximum value of the new matrix $\max(P')$:

$$P(i, j) = P'(i, j) \frac{\max(P)}{\max(P')}. \quad (8)$$

Figure 5 shows a sample T_M matrix, where Fig. 5(a) shows the initial sample matrix and Fig. 5(b) shows the matrix after smoothing.

1. The ignition interval: $[I_{\min}, I_{\max}]$

The fuel for the 12-m^2 prescribed burns was a mixture of live and dead needles, leaves, and brush and was gathered from the area designated for the fire, weighed, and then dispersed as evenly as possible throughout all 16 sections of each burn zone [40]. The 30-acre fires held a mixture of the same but more heterogeneously distributed. As ignition temperatures vary widely for these different fuels, we needed to find
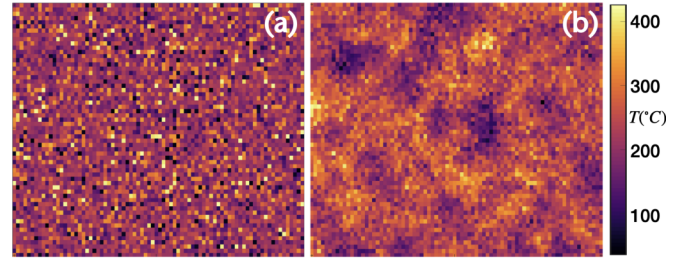

FIG. 5. A representative sample of T_M matrix and a smoothed version used in SERF: (a) initial T_M matrix with values sampled from the distribution for maximum temperatures; (b) T_M matrix after smoothing.

a reasonable interval, $[I_{\min}, I_{\max}]$, for ignition temperatures represented in these fires, $\{f_m\}_{m=1}^{74}$.

Since we had chosen the set of fires to be those known to ignite, we could estimate the second of ignition to be the time step at which the fire entered the field of view. Using visualizations of the infrared value tensors, we came up with an equation for the average temperature of the cells based on the maximum and minimum radiant temperature of each fire, f_m:

$$I_m(f_m) = |0.2[I_{\max}(f_m) - I_{\min}(f_m)]| + I_{\min}(f_m). \quad (9)$$

The equation was developed by finding the range of temperatures recorded in each fire f_m, $[I_{\min}(f_m), I_{\max}(f_m)]$, and determining the ignition point for that fire to be approximately 20% of that range above $I_{\min}(f_m)$. Then we found the greatest and least value for all ignition temperatures and that defined the ignition interval for SERF. Figure 6 shows the various temperatures for each fire in the data set.

From Fig. 6 we found that the minimum and maximum values for threshold for each of these fires to be $I_{\min} \approx 90\,°\text{C}$ and $I_{\max} \approx 150\,°\text{C}$. Note that Fig. 6 also shows the upper bound on the recording device at $400\,°\text{C}$ as described previously in Sec. III A.
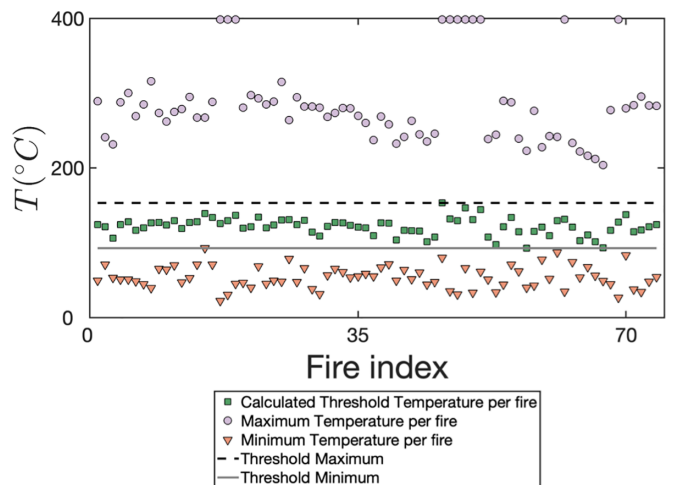

FIG. 6. Maximum, minimum, and threshold temperatures for each fire in degrees Celsius and the top and bottom of the threshold interval.
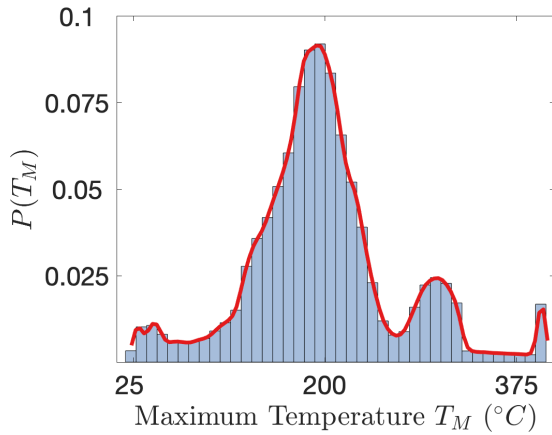
FIG. 7. Recorded maximum temperatures for 355,200 cells from all fires in the data set; histogram and fitted kernel distribution (red line).

2. Maximum temperatures

A kernel distribution was fitted to a histogram of the maximum radiant temperatures achieved for each cell in all of the fire tensors for a total of 355,200 cells. Figure 7 shows the maximum temperatures for each cell across all fires and the estimated distribution for these quantities. The majority of the fires had a large variance in temperatures across cells, resulting in various local maxima in the distribution. Moreover, there were some fires in which the entire area was engulfed in flames that all burned at the upper bound of the Lepton device. The tall bar at the right end of this graph in Fig. 7 represents these high-intensity fires. A large number of cells reached around 200°, indicating that most of the cells caught fire but did not release significant heat energy. The smaller local maxima around 300° indicates that certain fires maintained a higher temperature than average but did not reach the upper bound. In short, the variety of different fires begot various maximum temperatures.

This kernel distribution was then sampled to initialize all cells in the T_M parameter matrix. The "smoothing" process was then applied as described in Sec. III B. Each cell was "smoothed" to allow for more even heating temperatures in neighboring cells.

3. Rise (R) and fall (F) times distributions

Using the ignition temperature defined for each fire (see Sec. III B 1), we measured the number of time steps, $R(i, j)$, required for the temperature in each cell to go from the starting ignition temperature, $T_S(i, j)$, up to maximum temperature $T_M(i, j)$ and the number of time steps $F(i, j)$ to fall from $T_M(i, j)$ back to the ignition temperature. Figure 8 shows the distribution of R and F derived from the data. The red lines in this figure are the corresponding kernel density estimate. We experimented with various probability distributions including joint distributions for these parameters and found that the kernel distribution with each R and F value sampled separately produced results that most closely matched the data-set fires.

The average rise time, $\langle R \rangle = 26$ s, and the average fall time $\langle F \rangle = 58$ s. These histograms indicate a strong likelihood that
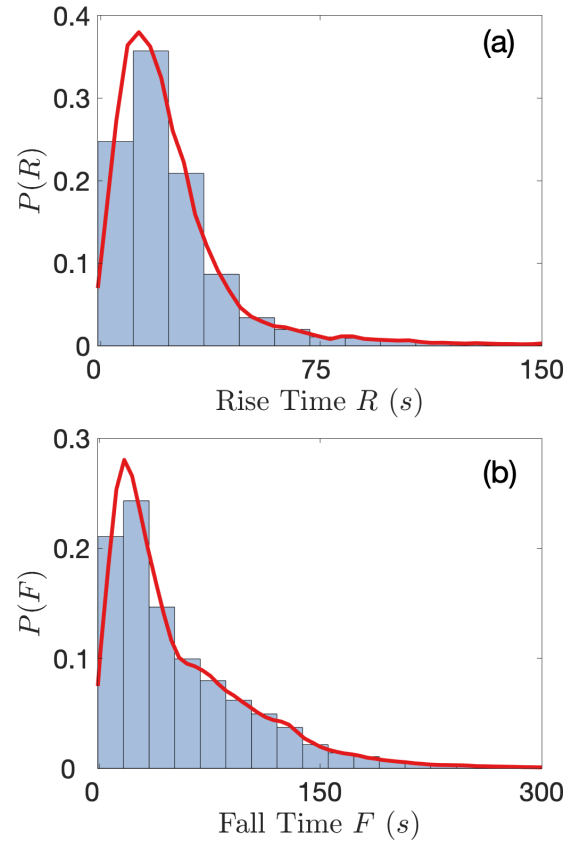

FIG. 8. Rise (a) and fall (b) time value histograms and kernel distributions from the data set.

the rise and fall times would be relatively low, although it is possible to have a long tail during the cooling stage.

4. Heat coefficient array (k-matrix)

The heat coefficient for a given material is typically determined as the likelihood of a given substance to transfer heat to a neighboring material. Sometimes referred to as "conductance," it is the primary parameter in Newton's law of cooling which was used for the rising of the temperature during stages one and two and the transition into stage three. We determined the probability distribution of these coefficients from the data set by finding the global maximum temperature achieved for all cells in a given fire and then estimating the ratio of the maximum temperature for each cell to that global value. This gave us a number between 0 and 1 that we used to represent the "burnability" of that particular cell. We created a histogram and fitted a kernel distribution to the data. Figure 9 shows the results of that distribution.

We note that the majority of the calculations of k lie between 0.7 and 0.95, which implies that the radiant temperatures for each cell were relatively close to the global maximum for that fire. This accounts for an approximate mean of 0.0855 for the unburnt proportion of land, U, and also indicates that most of the cells reached temperatures above $I_{\max}$. The values for the k parameter matrix are sampled from this probability distribution for each cell in the domain. The matrix is then "smoothed" according to the method described at the start of Sec. III B. As with the other cell-specific parameter matrices
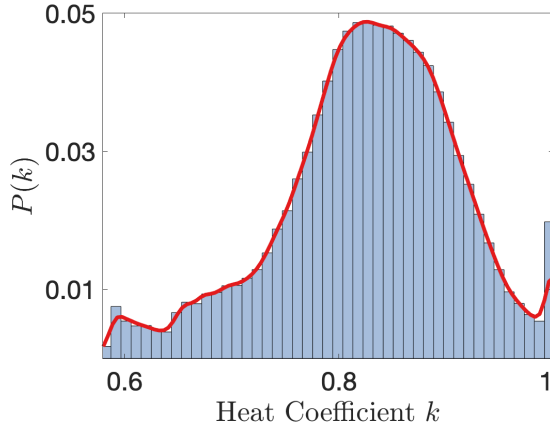
FIG. 9. Heat coefficient histogram with kernel distribution; found largest temperature value in the maximum temperature matrix for each fire and the proportion of that maximum reached by each cell.

(R, F, and T_M), we experimented with various probability distributions for these values but found the kernel distribution to represent the heat coefficients most accurately in comparison with the data set.

5. Initial conditions

From the visualizations of the data-set fires, we found four initial conditions represented: corner, side, chunk, and double chunk. Figure 10 shows examples of these initial conditions from the simulations alongside data-set representations of each type (the left images are from SERF simulations and the right from the data set). It should be noted that the orientation of the cameras was not standardized when they were placed along the truss, which means that the fire traveled in several directions on camera. For SERF, the fires all move in the same direction with a standardized trajectory of west to east or south to north within the view frame.

We also incorporated an initial condition that was not represented in the data set. It is widely known that spotting occurrences in wildfires can accelerate the spread of the fire [42,43], and understanding this phenomenon is an important part of keeping prescribed fires under control. Therefore, we added more simulations with a fifth initial condition of spotting, where we ignited three spots in the middle of the domain (see Fig. 11).

As described in Sec. II A 2, these initial conditions were used to synthetically raise the temperature of a particular set of cells at the start of the simulation. Each of these cells were raised to I_{max} for the CML model and the stages set to three in the CA model. The Appendix has examples of each ignition type from the data set and the simulations, including a set of images from the spotting ignition. Of note in these images are that the timing varied greatly for the length of the fires within the viewing area, but the simulation versus the data-set image sets are quite similar in structure.

6. Distribution for unburnt area

For verification purposes, we used the unburnt proportion of land in each fire from the data set, $U(f_m)$, by determining
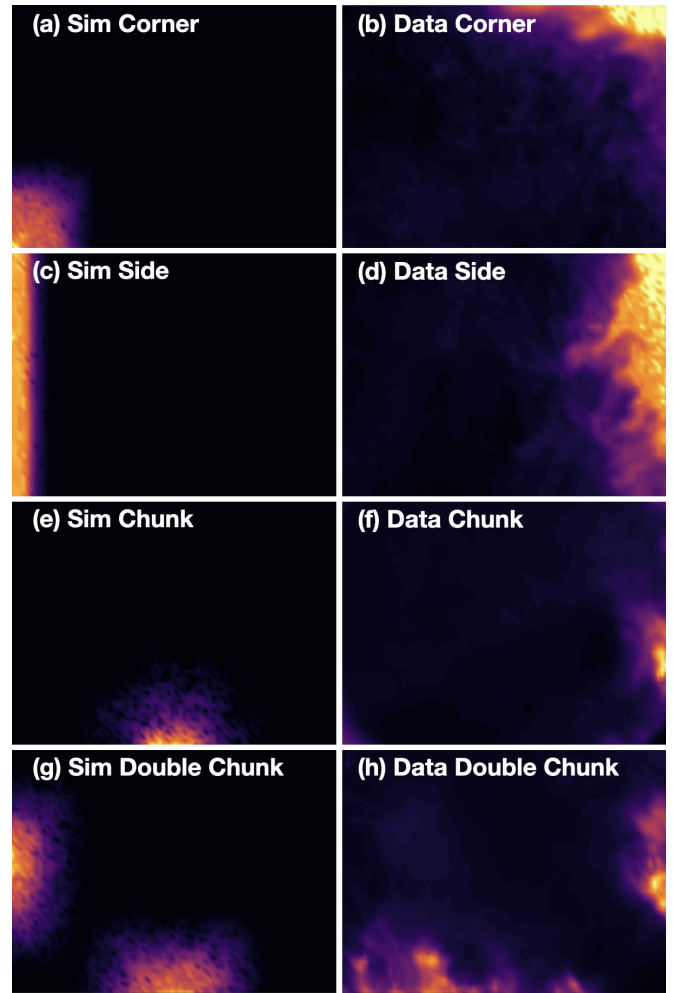

FIG. 10. Initial conditions: (a) corner from $\{S_m\}$, (b) corner from $\{f_m\}$, (c) side from $\{S_m\}$, (d) side from $\{f_m\}$, (e) chunk from $\{S_m\}$, (f) chunk from $\{f_m\}$, (g) double chunk from $\{S_m\}$, and (h) double chunk from $\{f_m\}$.
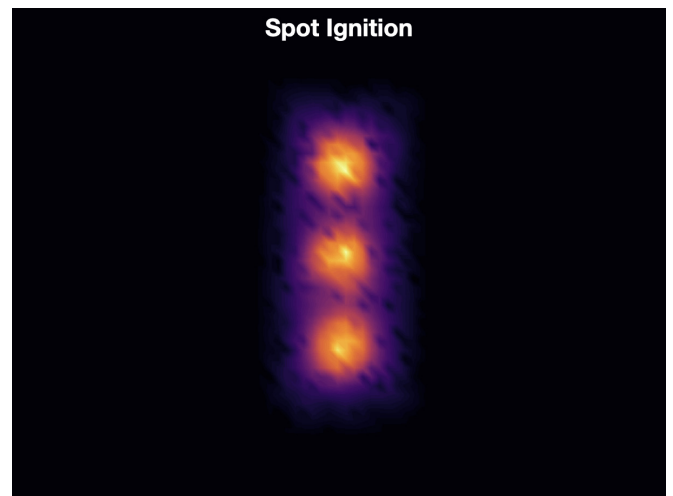

FIG. 11. Spotting initial condition added to the simulations to analyze fires beyond what was represented in the data set.
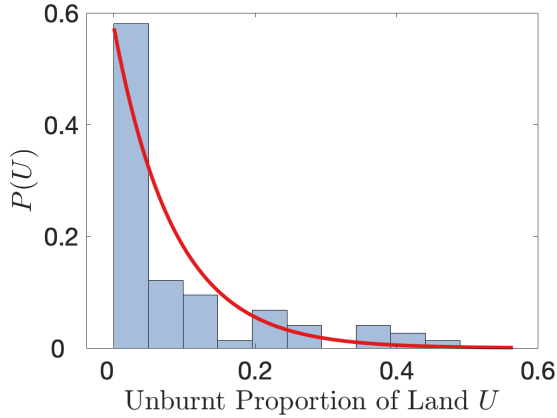
FIG. 12. Histogram of the proportion of cells that did not burn in each fire from the data set (U). The exponential curve fitted to the histogram shown here in red has a mean of $\langle U(f_m) \rangle = 0.0855$.

the mean, $\langle U(f_m) \rangle$, of this parameter (the mean is taken over $\{f_m\}_{m=1}^{74}$, the fire instances). To find the proportion of cells that did not ignite and therefore did not burn, we used the ignition values represented in Fig. 6 and described in Sec. III B 1 and defined each of the cells as burnt if they achieved the ignition temperature for that particular fire or unburnt if they did not. We counted the number of cells whose final state was burnt of the total number of cells in each fire and created a matching exponential distribution. Figure 12 shows the histogram with the fitted exponential. When we fit the curve for the proportion of land that did not burn, we found that $\langle U(f_m) \rangle = 0.0855$.

C. Non-data-driven parameter: Moisture content, m_c

Although moisture information was not available for the data set, fuel moisture levels have a major impact on fire behavior [44,45]. To appropriately use the moisture content in the simulations, we needed to associate that value, m_c, with whether the cell would ignite. To do this, we use this moisture level as a threshold to decide if the temperature will change for that cell for a given time step. For each cell, we randomly generate a uniformly distributed number between 0 and 1 and if the number is below m_c, then we set $T_{n+1}(i, j) = T_n(i, j)$ and the algorithm skips to the next cell. This allows for a slower rate of spread when the moisture level is higher.

When testing the effect of the moisture content in the simulations, we found that while this random uniform number had an effect, the speed of the fires in the data set were still slower than those achieved with m_c. Thus, to accentuate the effect of m_c, we created a parameter matrix to delay the ignition, $D(i, j)$, in which each cell was assigned an integer between 1 and 10 from a uniform distribution for how many times SERF attempts to ignite that particular cell. The matrix was then smoothed using the method described in Sec. III B and returned to integers. This delay value is used to test the transition from stage two to stage three. If the cell does not ignite within $D(i, j)$ attempts at ignition, then the cell is considered nonflammable and the algorithm transitions that cell from stage two directly into stage five, cooling. As with the other parameter matrices, this matrix was built by assigning

values as described above to all of the cells in each simulation and then "smoothing" the values across the domain.

IV. RESULTS AND DISCUSSION

We performed a total of 100 SERF simulations, $\{S_m\}_{m=1}^{100}$ with 20 of each initial conditions described in Sec. III B 5. A simulation begins with a synthetic rising of the temperature to $I_{\max}$ and setting the cell stage to three for a collection of cells. A simulation is considered complete when all cells have reached stage five. We collected the fire simulation tensors, parameter matrices, and a variety of other useful information from each simulation so that we could analyze the results. Since the data set was collected at 1-s intervals, each $I \times J$ matrix produced from the algorithm is considered to be 1 s in the life of the fire.

To verify SERF, we compared several metrics from the model simulations to the data set, including the likelihood of transition between stages, burning potential for each cell, the proportion of land that remained unburnt, and two timing metrics for spread rates. Each is described in detail in Sec. IV A.

To validate SERF, we compared the output to a typical CA model without the underlying CML model to show the strengths of adding the ability to achieve a continuous set of outputs for determining the states of the system. The results of these tests are described in detail in Sec. IV B.

A. Model verification

The combination of all of the probabilistic parameter inputs with the smoothing function described in Sec. III B, the uniformly distributed moisture content and delay matrix, and the stochastic values generated in the algorithm makes SERF inherently probabilistic. Thus, we were able to use several input parameter distributions as metrics to calibrate and verify the model. We ran several sets of simulations and compared the outputs to these parameters as metrics derived from the observational data. In particular, we compared unburnt areas $U(f_m)$ for each fire in $\{f_m\}_{m=1}^{74}$, the distribution of maximum temperatures, and the distributions of rising and fall times.

1. Transition matrices

To test the overall effectiveness of the CA model, we developed a transition matrix for the data-set fires $\{f_m\}_{m=1}^{74}$ and the SERF simulations $\{S_m\}_{m=1}^{100}$ showing the probability of moving from one stage to another, calculated and averaged over all cells in the fires and simulations separately. The transition matrices were then created for the fires and SERF. Figure 13 shows the difference between the transition probabilities for the fires and the SERF simulations.

Due to the probabilistic nature of the algorithm, each set of simulation results were unique in their comparison to the data set. Using the parameter values and ranges we chose, the resulting differences ranged from a maximum difference of 11% to 12% in transition from stages two to three. We have chosen to show a matrix representing an 11.76% maximum difference in Fig. 13. The rest of the differences were less than 3% for all sets of simulations indicating that SERF successfully captured the transition probabilities for each stage. Other metrics that were compared with the data set including unburnt
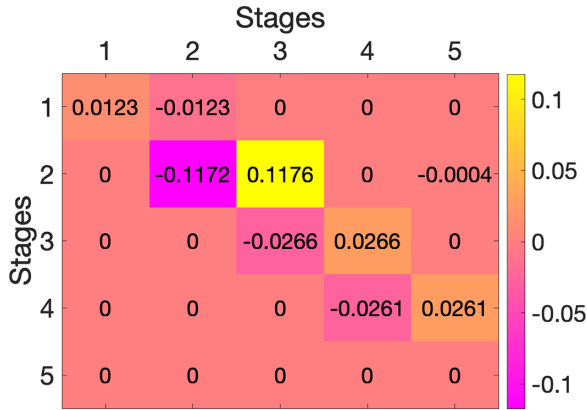
FIG. 13. Percentage differences in stage transition probabilities for the SERF simulations versus the data set. The simulations reproduce the transition probabilities with an error of less than 3% for all cases except the stage two to three transition where the error is 12%.

FIG. 15. Box plot showing the unburnt proportion of land in the SERF simulations compared to the data set. Observe the relative similarity between U in the data set and simulations.

proportion of land and the heat coefficient ranges showed no major changes between the various simulation runs.

2. Heat coefficients vegetation burning potential

The heat coefficients assigned to each cell represent the likelihood of the fuel burning. A low heat coefficient indicates a low probability of ignition, as in the case of a cell that is dominated by the presence of a rock or dirt, as opposed to leaves or branches, which would represent a higher heat coefficient. Initialized using the distribution from the data set as defined in Sec. III B 4, the final heat coefficients were also affected by the moisture content, m_c, and the delay matrix, D. Figure 14 shows the heat coefficients of each cell from every simulation in comparison to those determined from the data sets.

The mean of the heat coefficients for SERF is approximately 0.8351 and the mean for the data set is 0.8264, a difference of 0.0087. In Fig. 14, we observe that the variance of the simulations and data set are relatively close, and the median values represented by the red lines are 0.8325 and 0.8347

for the data set and simulations respectively, which indicates a difference of only 0.0022 and a successful representation of the heat coefficients for the data set in the model.

3. Unburnt proportion of land

Another metric we used to determine the success of SERF was to see if the unburnt proportion of land (U) was similar between the simulations and the data set. Figure 15 shows a box plot that exhibits the success of this metric. For SERF, we estimated U by finding the proportion of cells that transitioned from stage two to stage five without ignition. T_A, M, D, and k influenced U.

The mean of U in the SERF simulations is 0.0865, and in the data set 0.0867, for a difference of 0.0002. The medians (represented as the red line in the box plot) are 0.0293 and 0.0125 for the data set and simulations, respectively, which exhibits a difference of only 1.68%. The variance of U differed, with the simulations creating slightly more variance than the data set.

4. Lingering embers

Often in a fire, particular spots continue to burn long after the bulk of the fire has dissipated. This phenomenon has to do with the density and moisture level of the fuel on the ground. A more moisture-rich fuel takes longer to burn because the water must be evaporated off before the fuel can be consumed, and a denser area lacks the ability to draw in the oxygen as freely so the combustion process slows. Understanding the length of time embers may linger during a prescribed burn could inhibit the introduction of firebrands into the surrounding foliage long after the area has burnt. In the data set, 29 of the 74 fires showed obvious evidence of lingering embers. However, many of the data-set visualizations were cut short from the full length of the fire if the embers burned at a low temperature, so some lingering embers may have been lost.

Figures 16(a) and 16(b) shows some images from the data-set fires representing this phenomenon and Figs. 16(c) and 16(d) shows the same behavior from the simulations. In the SERF simulations, this originates from the probabilistically determined rise and fall times of each cell in conjunction with
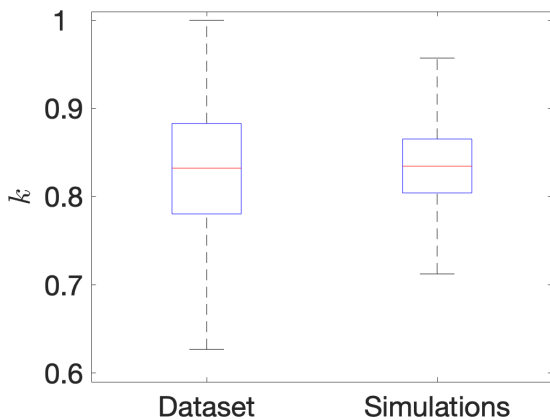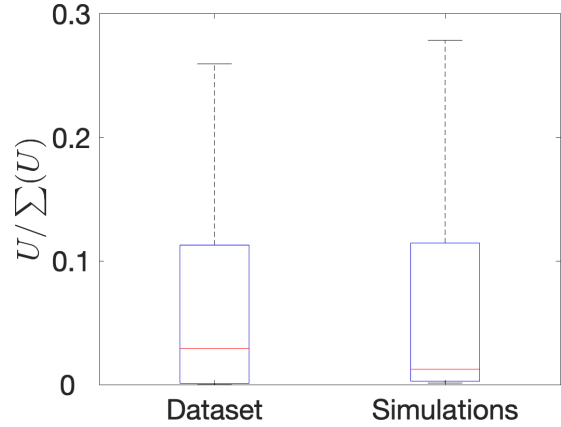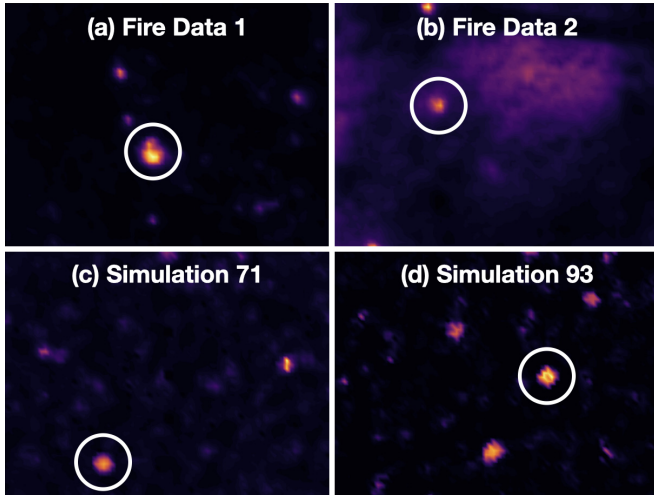

FIG. 14. Box plot comparing the heat coefficients in the SERF simulations and the data set; the red line in the middle of the boxes indicates median values. Observe the relative similarity between k in the data set and SERF simulations.

FIG. 16. Lingering embers in the simulations and fire data sets; (a) f_8, second 500 of 1100; (b) f_{50}, second 2550 of 2894; (c) S_{71}, second 2000 of 2310; (d) S_{93}, second 900 of 1241.

the varying start time for the ignitions. Some of those values add up to a long burn for a particular group of cells.

5. Cell rise and fall relationship with fireline

Many CA models focus on the speed of the fireline as it moves through the area because that gives an indication of how quickly it will take over a given area outside of the burn zone. However, the time the fire spends in any given area can also make a huge difference to fire practitioners because of the likelihood of firebrand transport, lingering embers, and smoke production. SERF accurately represents the variance in how long the fire spends in any given area. Figure 17 displays some stills from SERF simulation number 30 that exhibit the length of time the fire spends in the domain.

B. Model validation: Comparison to basic CA

To validate mathematical models, we compare the model output against known fire behavior and analyze any similarities or differences. For SERF, we made a direct comparison to
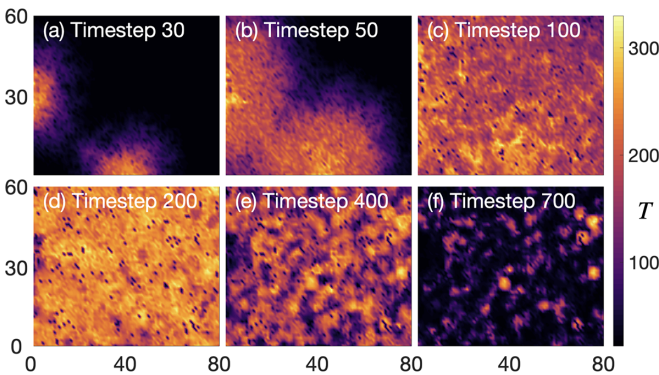

FIG. 17. Successful representation of the lingering heat after the fireline moves through the area; images from SERF simulation number 30; (a) time step 30; (b) time step 50; (c) time step 100; (d) time step 200; (e) time step 400; and (f) time step 700.
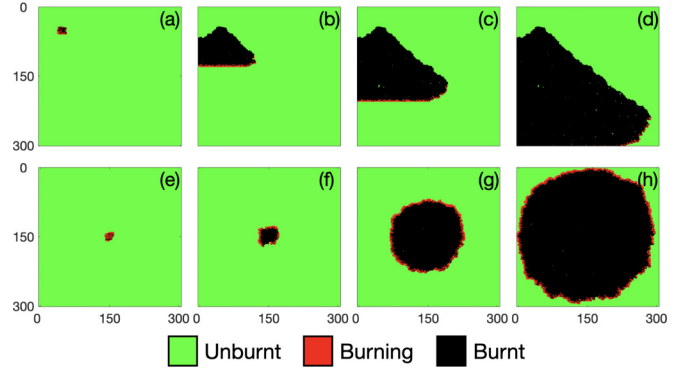

FIG. 18. The 300×300 grid for a basic CA model with probability of spread weighted by wind; [(a)–(d)] northern winds at 15 mph; (a) time step 5; (b) time step 75; (c) time step 150; (d) time step 250; [(e)–(h)] no winds; (e) time step 5; (f) time step 20; (g) time step 80; and (h) time step 150.

a much lower complexity CA model. We began this project by constructing our own basic square-cell CA model. For this basic model, each cell is in one of three states: burned, unburnt, or burning, so that $B_n(i, j) \in \{0, 1, 2\}$, respectively, for each cell, (i, j), and time step n. The only parameter represented in this basic CA model is a heat coefficient for each cell uniformly distributed between 0.5 and 1 such that $\forall (i, j), k(i, j) \sim \mathcal{U}(0.5, 1)$.

All cells are initialized with a value of unburnt, $\forall (i, j), B_0(i, j) = 1$. We "ignite" a fire by assigning a selection of cells to the burning stage, such that $B_0(i, j) = 2$ for those cells. With each time step in the loop, each cell that is currently burning may cause a neighboring cell to transition into the burning stage by a factor that is based on wind direction and speed. With wind speed $W = 0$ m/s, the factor governing any of the eight neighboring cells transitioning to burning is 0.5. With a wind speed greater than 0, the factor increases by $0.4 \times W/5$ in the direction of the wind, and $0.3 \times W/5$ for the neighboring cells to the wind direction, and reduces by $0.4 \times W/5$ in the opposite direction from the wind and $0.3 \times W/5$ for the neighboring cells in opposition to the wind direction. The cells perpendicular to the wind direction remain with a transition factor of 0.5. The 5 in the denominator for each of these values minimizes the effect of the wind for slower wind speeds below 5 m per second. For instance, if we set the wind direction to NW (meaning the wind is coming from the NW) and the wind speed to 5, then we have the following factor matrix for the neighboring cells of a particular cell $B_n(a, b)$ transitioning into the burning state:

$$\text{if} \quad B_n(a, b) = 2$$

$$\mathcal{F} \begin{bmatrix} (a-1, b+1) & (a, b+1) & (a+1, b+1) \\ (a-1, b) & (a, b) & (a+1, b) \\ (a-1, b-1) & (a, b-1) & (a+1, b-1) \end{bmatrix}$$

$$= \begin{bmatrix} 0.1 & 0.2 & 0.5 \\ 0.2 & 0 & 0.8 \\ 0.5 & 0.8 & 0.9 \end{bmatrix}. \tag{10}$$

The new values of the cells are then calculated as the sum of the originally assigned heat coefficient value described in the first paragraph with these factors above, and then we use the ceiling function to define the current state of cell (i, j) as 1 (unburnt) or 2 (burning):

$$B_n(i, j) = \lceil k(i, j) + \mathcal{F}(i, j) \rceil. \qquad (11)$$

If the cell value is unburnt ($B_n(i, j) = 1$), then the cell remains available for this transition in subsequent time steps. If the cell is burning, ($B_n(i, j) = 2$), then the cell will transition to 0 in the next time step and remain at 0 from there on. Thus, in each time step, each cell will achieve one of only three distinct states: 0,1, or 2. Once a cell has transitioned into burning, or state 2, the next time step transitions the cell into the burnt state, 0. Therefore, no cell remains burning for longer than one time step. The simulation ends when no cell values are equal to 2 or $\forall(i, j), B_n(i, j) \in \{0, 1\}$.

For comparison to SERF, Figs. 18(a)–18(d) shows different time steps from that basic model using a 300×300 grid with winds from the north at 5 mph, and Figs. 18(e)–18(h) showing the same domain with no winds.

From these figures, the fireline clearly defines the next movements through the field of view, and the presence of heavy winds adjusts the fireline significantly. With no winds, this basic CA model represents the elliptical shape of the fireline with concentric contours as portrayed in the other papers [5,29–36,46]. The main difference between this type of CA model and SERF is that the underlying CML model gives us more information regarding parameters other than the location of the fireline. SERF offers an opportunity to potentially learn about how the heat transfers from one area to the next and includes the time delay between when the fireline crosses through the area and when the fire is completed. These are important features of a prescribed fire to study in order to mitigate the potential for firebrands to be blown outside of the burn zone.

V. CONCLUSION

This paper describes and analyzes a SERF, combining a CA and CML framework, modeling radiant temperatures with data-driven parameters for fine-scale prescribed fire spread. Using a data set created in the New Jersey Pine Barrens over the course of 5 years, we built a cellular automata model using probability distributions for several parameters derived from the data set. The use of the data set is unique to SERF and helps to validate the accuracy of the model and simulations.

SERF uses a five-stage approach to how the radiant temperature changes through the life cycle of a given fuel cell. Stage one, stable, occurs before any temperature changes in the cell, and stage two represents the warming of each cell based on the radiant temperature of the surrounding eight cells. After ignition, stage three represents the rising of the radiant heat in the cell and stage four represents the falling of the heat after the fuel has been mostly consumed. The final stage represents the cooling off of the cell back to base temperature. This approach offers the opportunity to simplify the physical processes of fire behavior to save computational time while maintaining the relationships between stages of the burning process.

The significant contribution of this work is a data-driven cellular automata model supported by a coupled map lattice model that can accurately represent the speed of the fire as it moves through the area. Moreover, it can accurately capture the unburnt proportion of land in the SERF simulations, the presence of lingering embers, the heat coefficients of the fuel on the ground, and the probability of transition between stages.

While SERF has shown excellent performance in reproducing many of the features of prescribed fires, and it is one of the first nonlaboratory data-driven cellular automata models for prescribed fires, some parts of the model still need refinement. In future work, we plan to explore a variety of modifications to the model to increase its accuracy, as it under-performed in some critical parameter settings. We will perform a more advanced analysis of the SERF simulation outputs to assess how various parameters affect the model's accuracy. Furthermore, we will study the statistical properties of the spatial features of fire.

APPENDIX: OUTPUT IMAGES

Figures for each of the five ignition types are listed below. Figure 19 shows stills of the SERF simulations with a side ignition and Fig. 20 shows the side ignition from the data set. Figure 21 shows the SERF corner ignition and Fig. 22 shows the corner ignition from the data set. Figure 23 represents the chunk ignition from SERF with Fig. 24 showing the data set chunk ignition. Figures 25 and 26 show the double chunk ignition from SERF and the data set, respectively. Figure 27 shows the spotting ignition from the SERF simulations. Each set of images from the data represents six particular time steps from the fire data. Each set of images from the simulations
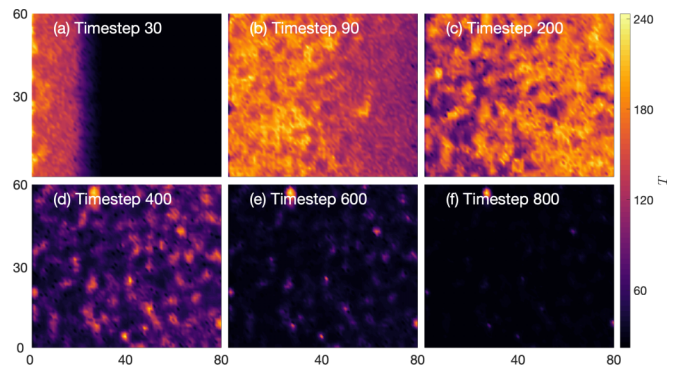

FIG. 19. Side ignition: Simulation 4; (a) time step 5; (b) time step 200; (c) time step 400; (d) time step 700; (e) time step 1000; and (f) time step 1300.

represents six time steps from the simulation. Of note within these images is the similarity between the data set and simulation ignition types. Although the timing of each varied greatly, looking at the images clearly shows the successful representation of this data set through this model.
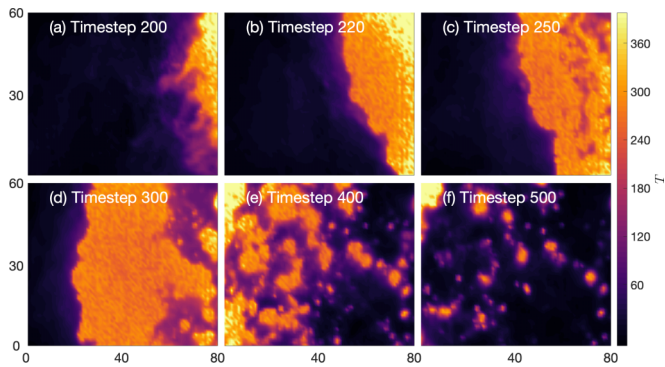

FIG. 20. Side ignition: Dataset Fire 120; (a) time step 200; (b) time step 220; (c) time step 250; (d) time step 300; (e) time step 400; and(f) time step 500.
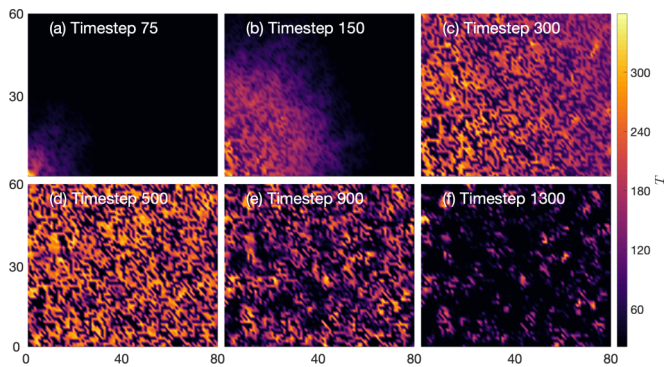

FIG. 21. Corner ignition: Simulation 25; (a) time step 75; (b) time step 150; (c) time step 300; (d) time step 500; (e) time step 900; and (f) time step 1300.
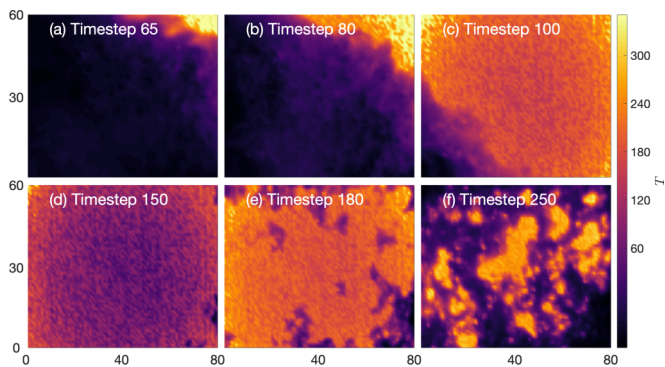

FIG. 22. Corner ignition: Dataset Fire 25; (a) time step 65; (b) time step 80; (c) time step 100; (d) time step 150; (e) time step 180; and (f) time step 250.
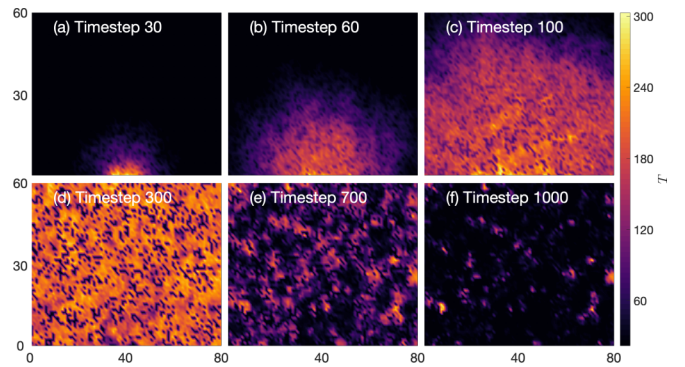

FIG. 23. Chunk ignition: Simulation 45; (a) time step 30; (b) time step 70; (c) time step 200; (d) time step 300; (e) time step 500; and (f) time step 700.
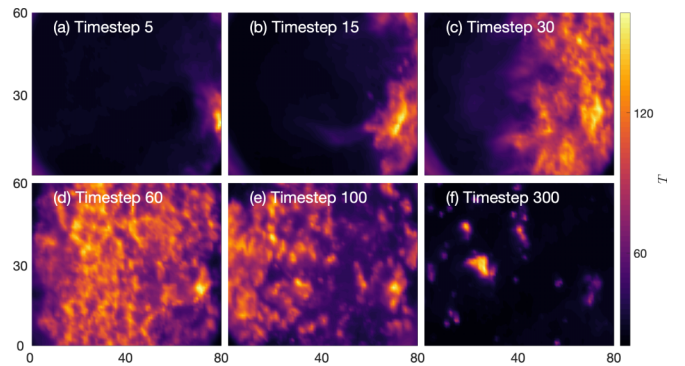

FIG. 24. Chunk ignition: Dataset Fire 145; (a) time step 5; (b) time step 15; (c) time step 30; (d) time step 60; (e) time step 100; and (f) time step 300.
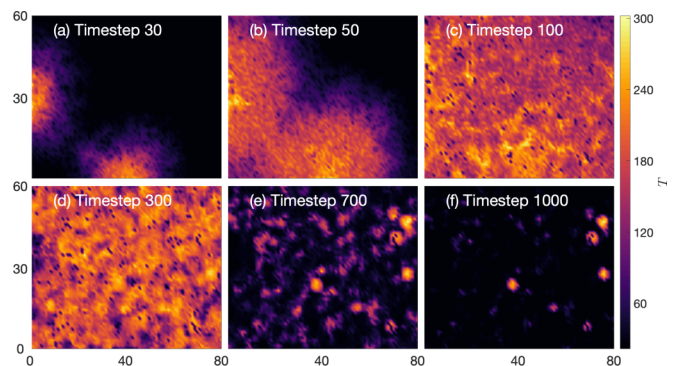

FIG. 25. Double Chunk ignition: Simulation 90; (a) time step 30; (b) time step 50; (c) time step 90; (d) time step 200; (e) time step 500; and (f) time step 800.
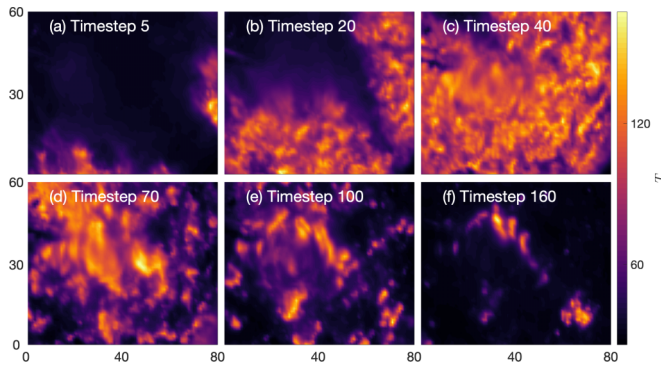
FIG. 26. Double Chunk ignition: Dataset Fire 3; (a) time step 5; (b) time step 20; (c) time step 40; (d) time step 70; (e) time step 100; and (f) time step 160.
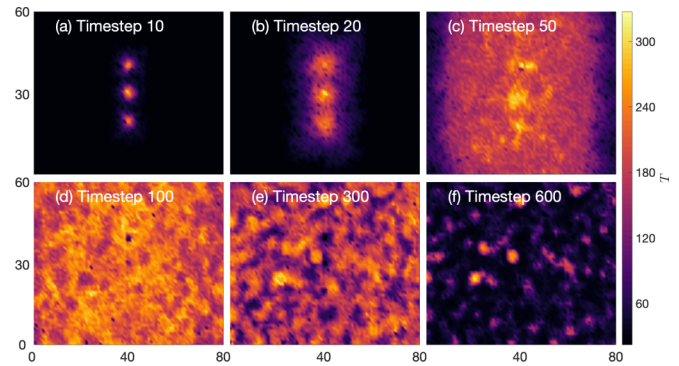

FIG. 27. Spotting ignition: Simulation 63; (a) time step 10; (b) time step 20; (c) time step 50; (d) time step 100; (e) time step 300; and (f) time step 600.

[1] J. T. Abatzoglou and A. P. Williams, Proc. Natl. Acad. Sci. USA **113**, 11770 (2016).

[2] S. W. Running, Science **313**, 927 (2006).

[3] *Wildfires and Acres* (National Interagency Fire Center, Boise, ID, 2022).

[4] D. E. Calkin, J. D. Cohen, M. A. Finney, and M. P. Thompson, Proc. Natl. Acad. Sci. USA **111**, 746 (2014).

[5] H. Mahmoud and A. Chulahwat, Proc. Eng. **198**, 1111 (2017).

[6] V. C. Radeloff, D. P. Helmers, H. A. Kramer, M. H. Mockrin, P. M. Alexandre, A. Bar-Massada, V. Butsic, T. J. Hawbaker, S. Martinuzzi, A. D. Syphard, and S. I. Stewart, Proc. Natl. Acad. Sci. USA **115**, 3314 (2018).

[7] G. Busenberg, Rev. Policy Res. **21**, 145 (2004).

[8] D. O. Carpenter, M. K. Taylor, M. A. Callaham, J. K. Hiers, E. L. Loudermilk, J. J. O'Brien, and N. Wurzburger, Ecosystems **24**, 1059 (2021).

[9] R. S. Arkle, D. S. Pilliod, and J. L. Welty, Forest Ecol. Manage. **276**, 174 (2012).

[10] T. J. Duff, J. G. Cawson, and T. D. Penman, Forest Ecol. Manage. **433**, 431 (2019).

[11] E. R. Gleim, G. E. Zemtsova, R. D. Berghaus, M. L. Levin, M. Conner, and M. J. Yabsley, Sci. Rep. **9**, 9974 (2019).

[12] K. G. Tolhurst and G. McCarthy, Austr. Forest. **79**, 1 (2016).

[13] M. W. Brunson and J. Evans, J. Forest. **103**, 134 (2005).

[14] J. Yoder, J. Law Econ. **51**, 297 (2008).

[15] R. Linn, J. Winterkamp, J. J. Colman, C. Edminster, J. D. Bailey, R. Linn, J. Winterkamp, J. J. Colman, C. Edminster, and J. D. Bailey, Int. J. Wildl. Fire **14**, 37 (2005).

[16] R. Linn, J. Reisner, J. J. Colman, and J. Winterkamp, Int. J. Wildl. Fire **11**, 233 (2002).

[17] R. R. Linn, S. L. Goodrick, S. Brambilla, M. J. Brown, R. S. Middleton, J. J. O'Brien, and J. K. Hiers, QUIC-fire: A fast-running simulation tool for prescribed fire planning, Environ. Model. Softw. **125**, 104616 (2020).

[18] W. Mell, J. Charney, M. A. Jenkins, P. Cheney, and J. Gould, in *Remote Sensing and Modeling Applications to Wildland Fires*, edited by J. J. Qu, W. T. Sommers, R. Yang, and A. R. Riebau (Springer, Berlin, 2013), pp. 209–225.

[19] Y. Perez-Ramirez, W. E. Mell, P. A. Santoni, J. B. Tramoni, and F. Bosseur, Fire Technol. **53**, 1795 (2017).

[20] M. A. Penick, R. V. Hoang, F. C. Harris Jr., S. M. Dascalu, T. J. Brown, W. R. Sherman, and P. A. McDonald, in *Proceedings of the Conference on High Performance Computing Systems (HPCS'07)* (Association for Computing Machinery, New York, 2007).

[21] S. Wolfram, Rev. Mod. Phys. **55**, 601 (1983).

[22] T. Toffoli, Physica D **10**, 117 (1984).

[23] G. Y. Vichniac, Physica D **10**, 96 (1984).

[24] K. Kronholm and K. W. Birkeland, Geophys. Res. Lett. **32** (2005).

[25] A. Herault, A. Vicari, A. Ciraudo, and C. Del Negro, Comput. Geosci. **35**, 1050 (2009).

[26] D. H. Rothman, Geophys. **53**, 509 (1988).

[27] R. Rebba, S. Mahadevan, and S. Huang, Reliability eng. sys. safety **91**, 1390 (2006).

[28] U. Braga-Neto, in *Mathematical Methods in Pattern and Image Analysis* (SPIE, Bellingham, WA, 2005), Vol. 5916, pp. 304–314.

[29] A. Alexandridis, D. Vakalis, C. I. Siettos, and G. V. Bafas, Appl. Math. Comput. **204**, 191 (2008).

[30] M. de Gennaro, Y. Billaud, Y. Pizzo, S. Garivait, J.-C. Loraud, M. El Hajj, and B. Porterie, Fire Safe. J. **91**, 872 (2017).

[31] T. Ghisu, B. Arca, G. Pellizzaro, and P. Duce, Environ. Model. Softw. **71**, 1 (2015).

[32] Z. Zheng, W. Huang, S. Li, and Y. Zeng, Ecol. Model. **348**, 33 (2017).

[33] L. Hernández Encinas, S. Hoya White, A. Martín del Rey, and G. Rodríguez Sánchez, Appl. Math. Model. **31**, 1213 (2007).

[34] S. Yassemi, S. Dragićević, and M. Schmidt, Ecol. Mode. **210**, 71 (2008).

[35] J. G. Freire and C. C. DaCamara, Nat. Hazards Earth Syst. Sci. **19**, 169 (2019).

[36] Y. Liu, H. Liu, Y. Zhou, and C. Sun, Environ. Model. Softw. **108**, 14 (2018).

[37] R. M. Almeida and E. E. N. Macau, J. Phys.: Conf. Ser. **285**, 012038 (2011).

[38] S. G. Berjak and J. W. Hearne, Ecol. Model. **148**, 133 (2002).

[39] G. A. Trunfio, D. D'Ambrosio, R. Rongo, W. Spataro, and S. Di Gregorio, ACM Trans. Model. Comput. Simul. **22**, 6 (2011).

[40] Personal interview on fire dynamics (2019).

[41] FLIR Lepton 1.6 Engineering Data Sheet (2018).

[42] S. L. Manzello, S. Suzuki, M. J. Gollner, and A. C. Fernandez-Pello, Prog. Energy Combust. Sci. **76**, 100801 (2020).

[43] E. Koo, R. R. Linn, P. J. Pagni, C. B. Edminster, E. Koo, R. R. Linn, P. J. Pagni, and C. B. Edminster, Int. J. Wildland Fire **21**, 396 (2012).

[44] L. G. Blauw, N. Wensink, L. Bakker, R. S. P. van Logtestijn, R. Aerts, N. A. Soudzilovskaia, and J. H. C. Cornelissen, Ecol. Evol. **5**, 3830 (2015).

[45] F. T. P. Torres, J. M. N. Romeiro, A. C. d. A. Santos, R. R. de Oliveira Neto, G. S. Lima, and J. C. Zanuncio, Sci. Total Environ. **631-632**, 1304 (2018).

[46] P. Progias and G. C. Sirakoulis, Math. Comput. Model. **57**, 1436 (2013).